

# 3D printed hollow core terahertz Bragg waveguides with defect layers for surface sensing applications

JINGWEN LI, KATHIRVEL NALLAPPAN, HICHEM GUERBOUKHA, AND MAKSIM SKOROBOGATIY\*

*École Polytechnique de Montréal, Montreal, Québec H3C3A7, Canada*  
\*maksim.skorobogatiy@polymtl.ca

**Abstract:** We study a 3D-printed hollow core terahertz (THz) Bragg waveguide for resonant surface sensing applications. We demonstrate theoretically and confirm experimentally that by introducing a defect in the first layer of the Bragg reflector, thereby causing anticrossing between the dispersion relations of the core-guided mode and the defect mode, we can create a sharp transmission dip in the waveguide transmission spectrum. By tracking changes in the spectral position of the narrow transmission dip, one can build a sensor, which is highly sensitive to the optical properties of the defect layer. To calibrate our sensor, we use PMMA layers of various thicknesses deposited onto the waveguide core surface. The measured sensitivity to changes in the defect layer thickness is found to be 0.1 GHz/ $\mu\text{m}$ . Then, we explore THz resonant surface sensing using  $\alpha$ -lactose monohydrate powder as an analyte. We employ a rotating THz Bragg fiber and a semi-automatic powder feeder to explore the limit of the analyte thickness detection using a surface modality. We demonstrate experimentally that powder layer thickness variations as small as 3 $\mu\text{m}$  can be reliably detected with our sensor. Finally, we present a comparative study of the time-domain spectroscopy versus continuous wave THz systems supplemented with THz imaging for resonant surface sensing applications.

© 2017 Optical Society of America

**OCIS codes:** (060.2370) Fiber optics sensors; (040.2235) Far infrared or terahertz; (160.5298) Photonic crystals.

---

## References and links

1. M. Zourob, S. Elwary, and A. Turner, *Principles of bacterial detection: biosensors, recognition receptors and microsystems* (Springer, 2008).
2. X. D. Wang and O. S. Wolfbeis, "Fiber-optic chemical sensors and biosensors," *Anal. Chem.* **85**(2), 487–508 (2013).
3. X. Fan, I. M. White, S. I. Shopova, H. Zhu, J. D. Suter, and Y. Sun, "Sensitive optical biosensors for unlabeled targets: a review," *Anal. Chim. Acta* **620**(1-2), 8–26 (2008).
4. J. Li, H. Qu, and M. Skorobogatiy, "Simultaneous monitoring the real and imaginary parts of the analyte refractive index using liquid-core photonic bandgap Bragg fibers," *Opt. Express* **23**(18), 22963–22976 (2015).
5. W. B. Ji, S. C. Tjin, B. Lin, and C. L. Ng, "Highly sensitive refractive index sensor based on adiabatically tapered microfiber long period gratings," *Sensors (Basel)* **13**(10), 14055–14063 (2013).
6. A. Iadicicco, D. Paladino, S. Campopiano, W. J. Bock, A. Cutolo, and A. Cusano, "Evanescent wave sensor based on permanently bent single mode optical fiber," *Sens. Actuators B Chem.* **155**(2), 903–908 (2011).
7. A. Dudus, R. Blue, and D. Uttamchandani, "Comparative study of microfiber and side-polished optical fiber sensors for refractometry in microfluidics," *IEEE Sens. J.* **13**(5), 1594–1601 (2013).
8. M. P. DeLisa, Z. Zhang, M. Shiloach, S. Pilevar, C. C. Davis, J. S. Sirkis, and W. E. Bentley, "Evanescent wave long-period fiber bragg grating as an immobilized antibody biosensor," *Anal. Chem.* **72**(13), 2895–2900 (2000).
9. A. Hassani and M. Skorobogatiy, "Photonic crystal fiber-based plasmonic sensors for the detection of biolayer thickness," *J. Opt. Soc. Am. B* **26**(8), 1550–1557 (2009).
10. A. Mazhorova, A. Markov, A. Ng, R. Chinnappan, O. Skorobogata, M. Zourob, and M. Skorobogatiy, "Label-free bacteria detection using evanescent mode of a suspended core terahertz fiber," *Opt. Express* **20**(5), 5344 (2012).
11. B. You, J. Y. Lu, J. H. Liou, C. P. Yu, H. Z. Chen, T. A. Liu, and J. L. Peng, "Subwavelength film sensing based on terahertz anti-resonant reflecting hollow waveguides," *Opt. Express* **18**(18), 19353–19360 (2010).
12. C. H. Lai, B. You, J. Y. Lu, T. A. Liu, J. L. Peng, C. K. Sun, and H. C. Chang, "Modal characteristics of antiresonant reflecting pipe waveguides for terahertz waveguiding," *Opt. Express* **18**(1), 309–322 (2010).
13. B. You and J. Y. Lu, "Remote and in situ sensing products in chemical reaction using a flexible terahertz pipe waveguide," *Opt. Express* **24**(16), 18013–18023 (2016).

14. B. You, J. Y. Lu, C. P. Yu, T. A. Liu, and J. L. Peng, "Terahertz refractive index sensors using dielectric pipe waveguides," *Opt. Express* **23**, 27204–27212 (2015).
15. R. Singh, W. Cao, I. A. Naib, L. Cong, W. Withayachumnankul, and W. Zhang, "Ultrasensitive terahertz sensing with high-Q Fano resonances in metasurfaces," *Appl. Phys. Lett.* **105**(17), 171101 (2014).
16. R. Singh, A. I. Al-Naib, M. Koch, and W. Zhang, "Sharp Fano resonances in THz metamaterials," *Opt. Express* **19**(7), 6312–6319 (2011).
17. L. Chen, Y. Wei, X. Zang, Y. Zhu, and S. Zhuang, "Excitation of dark multipolar plasmonic resonances at terahertz frequencies," *Sci. Rep.* **6**, 22027 (2016).
18. J. Li, H. Qu, and M. Skorobogatiy, "Squeezed hollow-core photonic Bragg fiber for surface sensing applications," *Opt. Express* **24**(14), 15687–15701 (2016).
19. P. Chen, G. A. Blake, M. C. Gaidis, E. R. Brown, K. A. McIntosh, S. Y. Chou, M. I. Nathan, and F. Williamson, "Spectroscopic applications and frequency locking of THz photomixing with distributed Bragg-reflector diode lasers in low-temperature-grown GaAs," *Appl. Phys. Lett.* **71**(12), 1601–1603 (1997).
20. S. G. Johnson, M. Ibanescu, M. Skorobogatiy, O. Weisberg, T. D. Engeness, M. Soljacic, S. A. Jacobs, J. D. Joannopoulos, and Y. Fink, "Low-loss asymptotically single-mode propagation in large-core OmniGuide fibers," *Opt. Express* **9**(13), 748–779 (2001).
21. A. Argyros, I. M. Bassett, M. A. Eijkelenborg, and M. C. J. Large, "Analysis of ring-structured Bragg fibres for single TE mode guidance," *Opt. Express* **12**(12), 2688–2698 (2004).
22. M. Skorobogatiy and J. Yang, *Fundamentals of photonic crystal guiding* (Cambridge University, 2009).
23. T. D. Engeness, M. Ibanescu, S. G. Johnson, O. Weisberg, M. Skorobogatiy, S. Jacobs, and Y. Fink, "Dispersion tailoring and compensation by modal interactions in OmniGuide fibers," *Opt. Express* **11**(10), 1175–1196 (2003).
24. S. Dasgupta, B. P. Pal, and M. R. Shenoy, "Design of dispersion-compensating Bragg fiber with an ultrahigh figure of merit," *Opt. Lett.* **30**(15), 1917–1919 (2005).
25. A. Dupuis, A. Mazhorova, F. Desevedavy, M. Roze, and M. Skorobogatiy, "Spectral characterization of porous dielectric subwavelength THz fibers fabricated using a microstructured molding technique," *Opt. Express* **18**(13), 13813–13828 (2010).
26. M. Naftaly and R. E. Miles, "Terahertz time-domain spectroscopy for material characterization," *Proc. IEEE* **95**(8), 1658–1665 (2007).
27. E. Pickwell and V. P. Wallace, "Biomedical applications of terahertz technology," *J. Phys. D Appl. Phys.* **39**(17), R301–R310 (2006).
28. F. Ellrich, T. Weinland, D. Molter, J. Jonuscheit, and R. Beigang, "Compact fiber-coupled terahertz spectroscopy system pumped at 800 nm wavelength," *Rev. Sci. Instrum.* **82**(5), 053102 (2011).
29. M. Yahyapour, N. Vieweg, A. Roggenbuck, F. Rettich, O. Cojocari, and A. Deninger, "A Flexible phase-insensitive system for broadband CW-terahertz spectroscopy and imaging," *IEEE Trans. Terahertz Sci. Technol.* **6**, 670–673 (2016).
30. A. Roggenbuck, K. Thirunavukkuarasu, H. Schmitz, J. Marx, A. Deninger, I. C. Mayorga, R. Güsten, J. Hemberger, and M. Grüninger, "Using a fiber stretcher as a fast phase modulator in a continuous wave terahertz spectrometer," *J. Opt. Soc. Am. B* **29**(4), 614–620 (2012).
31. R. Mendis, V. Astley, J. Liu, and D. M. Mittleman, "Terahertz microfluidic sensor based on a parallel-plate waveguide resonant cavity," *Appl. Phys. Lett.* **95**(17), 171113 (2009).
32. R. Mendis and D. M. Mittleman, "Comparison of the lowest-order transverse-electric and transverse-magnetic modes of the parallel-plate waveguide for terahertz pulse applications," *Opt. Express* **17**(17), 14839–14850 (2009).
33. A. L. Bingham and D. Grischkowsky, "Terahertz two-dimensional high-Q photonic crystal waveguide cavities," *Opt. Lett.* **33**(4), 348–350 (2008).
34. C. M. Yee and M. S. Sherwin, "High-Q terahertz microcavities in silicon photonic crystal slabs," *Appl. Phys. Lett.* **94**(15), 154104 (2009).
35. A. Roggenbuck, H. Schmitz, A. Deninger, I. C. Mayorga, J. Hemberger, R. Güsten, and M. Grüninger, "Coherent broadband continuous wave terahertz spectroscopy on solid-state samples," *New J. Phys.* **12**(4), 043017 (2010).
36. K. S. Lee, T. M. Lu, and X. C. Zhang, "Tera tool," *IEEE Circuits Devices Mag.* **18**, 23–28 (2002).
37. H. B. Liu, G. Plopper, S. Earley, Y. Chen, B. Ferguson, and X. Zhang, "Sensing minute changes in biological cell monolayers with THz differential time-domain spectroscopy," *Biosens. Bioelectron.* **22**(6), 1075–1080 (2007).
38. W. Withayachumnankul, J. F. O'Hara, W. Cao, I. A. Naib, and W. Zhang, "Limitation in thin-film sensing with transmission-mode terahertz time-domain spectroscopy," *Opt. Express* **22**(1), 972–986 (2014).
39. K. Kawase, Y. Ogawa, Y. Watanabe, and H. Inoue, "Non-destructive terahertz imaging of illicit drugs using spectral fingerprints," *Opt. Express* **11**(20), 2549–2554 (2003).
40. J. F. Federici, B. Schulkin, F. Huang, D. Gary, R. Barat, F. Oliveira, and D. Zimdars, "THz imaging and sensing for security applications—explosives, weapons and drugs," *Semicond. Sci. Technol.* **20**(7), S266–S280 (2005).
41. W. Withayachumnankul and M. Naftaly, "Fundamentals of measurement in terahertz time-domain spectroscopy," *J. Infrared Millim. Terahertz Waves* **35**(8), 610–637 (2014).
42. P. U. Jepsen, D. G. Cooke, and M. Koch, "Terahertz spectroscopy and imaging—modern techniques and applications," *Laser Photonics Rev.* **5**(1), 124–166 (2011).

43. T. Ma, H. Guerboukha, M. Girard, A. D. Squires, R. A. Lewis, and M. Skorobogatiy, "3D printed hollow-core terahertz optical waveguides with hyperuniform disordered dielectric reflectors," *Adv. Opt. Mater.* **6**, 1 (2016).
  44. P. Kužel, H. Němec, F. Kadlec, C. Kadlec, P. Kuzel, H. Nemeč, F. Kadlec, and C. Kadlec, "Gouy shift correction for highly accurate refractive index retrieval in time-domain terahertz spectroscopy," *Opt. Express* **18**(15), 15338–15348 (2010).
- 

## 1. Introduction

Optical fibers have been extensively studied for biochemical sensing applications due to numerous advantages, such as small footprint, high degree of integration, and continuously quantitative and qualitative analysis. To date, a wide range of fiber-optic biochemical sensors based on various configurations have been proposed and developed [1–4]. One common fiber-based implementation for surface sensing is using an evanescent coupling of the total internal reflection (TIR) guided modes to the analyte layer. This sensing strategy has been applied in various configurations, such as tapered microfibers [5], U-shaped fiber [6] and side-polished fiber [7], as well as long period fiber grating (LPFG) [8]. Another popular implementation of the fiber sensors for surface sensing is based on the phenomenon of surface plasmon resonance (SPR). However, the probing length of those surface waves in the visible range is only on the order of 100nm [9], which limits its utility when trying to detect of larger targets (such as bacteria with sizes of 0.5 $\mu$ m-10 $\mu$ m).

In order to extend the probing depth of the surface waves to longer distances for macromolecular or bacteria detection, one can pursue biosensors operating at longer wavelengths (such as THz). For example, in [10], the authors used a suspended-core polyethylene THz waveguide for the detection of *E. coli* bacteria based on an amplitude modality. Selective binding of the *E. coli* bacteria to the surface of the waveguide core modifies the THz transmission properties of the suspended core waveguide due to enhanced scattering and absorption losses. Changes in the waveguide propagation loss can then be correlated to the concentration of the bacteria in the liquid analyte. Hollow tubes or dielectric pipes based on the anti-resonant reflecting optical waveguide (ARROW) mechanism [11–14] constitute an alternative to the THz micro-structured waveguide sensors based on the amplitude modality. The strongly localized THz evanescent wave enables detection of the subwavelength-thick analyte layers attached to the inner surface of the hollow tube. By tracking the spectral shift of the resonant wavelength, one can monitor changes in the analyte layer thickness. However, most of those sensors typically have relatively broad spectral features, which dramatically reduce the sensitivity and detection limit.

By employing sensors with narrow resonances, much higher sensitivities could be achieved. For example, in [15, 16], the authors demonstrated thin film sensing by exciting high-Q Fano resonances in planar terahertz metamaterials. Metamaterial structures have the advantage of being able to support resonances at any desired frequency based on their structural geometry, and these resonances are responsive to the changes in the thickness and the effective refractive index at their surface. Such resonances with extremely narrow linewidths enable measuring minute spectral shift caused by small changes in the thickness and refractive index of the surrounding media. In another example [17], multipolar plasmonic resonances at terahertz frequencies have been reported for designing ultra-sensitive sensors.

In this work, the relatively broad transmission spectrum of Bragg waveguide (45GHz) is modified by introducing a narrow spectral loss peak (3GHz). This is accomplished by introducing a geometrical defect in the first layer of the Bragg reflector. The spectral position of the loss peak is found to be highly sensitive to the optical properties of the defect layer, such as thickness and refractive index. The present work is inspired by our recent report using hollow-core Bragg fiber operating in the visible range for surface sensing applications [18]. It was demonstrated that a thin analyte layer deposited on the inner surface of the fiber core results in avoided crossing in the vicinity of the phase matching wavelength between the core-guided mode and the analyte layer bound mode. The wavelength of anticrossing, and as a

consequence, fiber transmission spectra is strongly dependent on the analyte layer thickness, thus allowing monitoring of changes in the analyte layer thickness.

In order to improve the detection limit of such sensors, we employ a THz Bragg waveguide operating in an effectively single mode regime. By directly tracking the anticrossing frequency between the core-guided mode and the defect mode, which manifests itself as a sharp transmission dip within the relatively broad transmission window, we have significantly improved the detection limit compared to the THz waveguide sensors reported in the literature [11–14]. In order to realize such sensors operating in the THz range, we use 3D stereolithography. The Bragg waveguide used in this work features a hollow core surrounded by a periodic sequence of high- and low-refractive index multilayers, namely, printing resin (PlasClear, Asiga) and air. The thickness of each bilayer is  $512\mu\text{m}$ , with a predicted fundamental bandgap centered at  $0.18\text{THz}$ . The waveguide core size of  $4.5\text{mm}$  is chosen to ensure an effectively single mode operation within the fundamental bandgap region. In order to introduce a transmission dip with narrow linewidth inside of the original bandgap, we increase the thickness of the first layer in the Bragg reflector, thus introducing anticrossing (hybridization) between the core-guided mode and the lossy modes confined in the vicinity of the defect layer. For sensor calibration, we use PMMA films with different thicknesses attached to the inner surface of the waveguide core. Then, an example of THz resonant surface sensing using  $\alpha$ -lactose monohydrate powder as the analyte is demonstrated experimentally. Simulations based on the finite element method (FEM) are conducted to validate the experimental results. The anticrossing phenomenon between the core-guided mode and defect mode is confirmed by imaging the modes propagated in the waveguide using a fiber-coupled THz microscopy setup. The Bragg waveguide sensor is characterized using both time domain spectroscopy (TDS) and continuous wave (CW) spectroscopy setup, and we conclude that the CW setup with higher frequency resolution is more suitable for applications that require high sensitivities. The ability to tailor the spectral properties of the sensors by properly designing their geometric parameters means that our Bragg waveguides become a viable platform for a wide range of application, such as detection of molecular and bacterial interactions, study of surface kinetics, monitoring of powder analytes, etc.

It is important to highlight several advantages of the proposed sensing system, which uses resonant phenomenon in the THz waveguides versus more traditional ways for layer thickness and composition monitoring such as the free space transmission mode spectroscopy. In particular, compared to the free space transmission mode spectroscopy which monitors thin film properties by observing the phase variations in the THz wave passing through an analyte film, our waveguide sensor rather uses resonant interaction between its various guided and leaky modes in the analyte layer while employing an amplitude (not phase) detection modality. Amplitude detection requires considerably simpler (and cheaper) THz systems, at the same time, offer a comparable sensitivity compared to the state-of-the-art phase detection modality employed in the free space transmission mode spectroscopy. This is the major advantage for the development of practical THz systems for industrial monitoring and sensing applications. Secondly, we note that most of the current resonant THz sensors have relatively broad spectral features, thus, resulting in lower sensitivities. In our photonic bandgap THz waveguide-based sensors, the modal field in the hollow core is resonantly coupled to the field in the defect mode concentrated in the analyte layer. This coupling is strongly wavelength dependent as it relies on the modal anticrossing phenomenon. Moreover, the strength of the intermodal coupling (hence, the spectral width of the transmission peak) can be designed to be as small as desired by simply displacing the analyte layer into the reflector region away from the core. As a result, the resonant dip with narrow linewidth in the waveguide transmission spectrum can be used to resolve minute spectral shifts in the resonant dip positions caused by small changes in the defect layer thickness or refractive index, which allows an improved detection limit, compared other conventional setups. Note that in our system detection sensitivity is fundamentally limited only by the spectral resolution of the

detector rather than by that of the resonant waveguide sensor. In particular, we demonstrate that for the same waveguide sensor designed to feature a  $\sim 3$ GHz transmission dip, when employing a CW THz system that offers sub-GHz spectral resolution, we get considerably higher detection sensitivities compared to the case of using a standard TDS-THz system with  $>3$ GHz resolution. We note that, by using a CW THz setup [19] capable of 4MHz spectral resolution, the waveguide sensors discussed in this paper can be, in principle, designed for the detection of sub-100nm changes in the layer thickness. To our knowledge, this is virtually impossible to achieve with other more standard approaches. Thirdly, we note that waveguide-based sensing system offers an opportunity for seamless integration of various conduits for the delivery of analytes (e.g. liquids, powders, gases) into the optical setup. As an example, in this work, we demonstrate that the spinning hollow core waveguide with minor modifications in its geometry can be used to produce (via centrifugal force) and hold thin layers of powders for the detection of changes in their mass (thickness), which, to our best knowledge, has never been reported before. This sensing strategy is especially relevant for many practical applications, such as environmental monitoring, among others applications. Finally, we note that by adjusting the waveguide geometry, one can target specific frequency range of interest, and enrich the sensing scenarios. For example, as proposed in our manuscript, by designing the operation frequency of the sensor near the absorption peak of  $\alpha$ -lactose monohydrate (at 0.53THz), one can simultaneously monitor the layer thickness and the lactose concentration in the powders using the anticrossing frequency and the absorption peak strength, respectively. Again, to our knowledge, this multi-parameter sensing modality has never been reported before, and it is beneficial for the design of versatile, and highly integrated sensors, which enables a comprehensive multi-parameter material characterization by a single device.

## 2. Design of an effectively single-mode THz Bragg waveguide

Single-mode operation gives many advantages for signal processing and sensing applications. The  $HE_{11}$  mode in a Bragg fiber has a Gaussian-like field distribution, and is generally favored over the lowest loss  $TE_{01}$  mode [20,21], because the  $HE_{11}$  mode can be easily excited with a linearly polarized THz input beam. In this section, we start by designing a THz Bragg waveguide operating in an effectively single mode regime.

Figure 1(a) shows the cross section of the waveguide used in our work, which features a hollow core surrounded by a periodic sequence of high/low refractive index multilayers, namely, the printing resin and air. The thickness of each layer is designed to be  $512\mu\text{m}$ , with a predicted fundamental bandgap center at 0.18THz, according to the basic theory of Bragg fibers [22]. This frequency region is chosen due to the following reasons: first, there are no water vapor absorption lines in this region, and waveguide sensors operating in this range are, therefore, less influenced by the environmental conditions; second, a single mode Bragg waveguide operating in this frequency range (the corresponding wavelength is around 1.5mm) has a relatively large core size, which is an asset for practical sensing applications, as it simplifies the introduction of analyte into the waveguide core. Moreover, a relatively large waveguide core size is also essential for the efficient coupling of THz beams. The number of the bilayers in the Bragg reflector is ten. In order to maintain the mechanical stability of the Bragg reflector, a set of micro-bridges are introduced into the waveguide cross section, as indicated in Fig. 1(a). In order to guarantee consistent alignment of the Bragg waveguide sections during the cutback measurements, U-shaped holders (see below) are used.

The most straightforward method to achieve an effectively single-mode operation is to reduce the waveguide core diameter until only one core-guided mode is supported. Reduction in the core size results in increase in the waveguide propagation loss, because the fields of the guided modes extend more into the waveguide cladding. Thus, not only the radiation loss due to finite number of bilayers in the reflector, but also the absorption loss due to the loss in the cladding material has to be considered. In order to achieve an effectively single-mode operation at the fundamental bandgap, we compute the band diagram of the Bragg waveguide

at different core diameters using a commercial finite element software COMSOL. We note that the Bragg waveguide used in this section features a perfectly periodic reflector (no defect layer). For the frequency dependent refractive index and absorption loss of the reflector material, we use the polynomial fits in Eq. (2) and Eq. (3) (See Appendix).

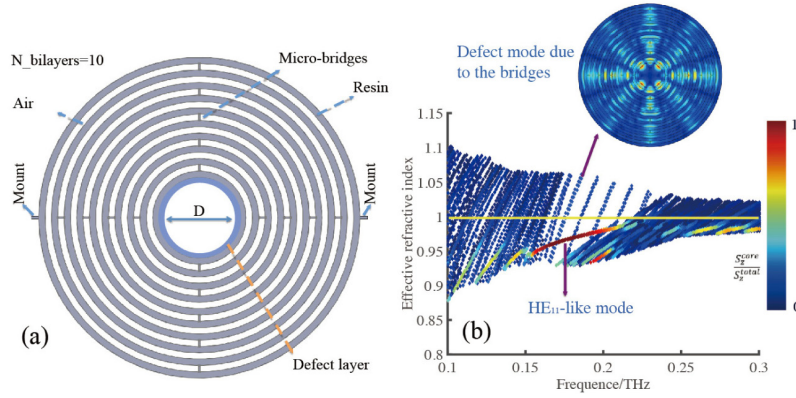


Fig. 1. (a) Schematic of the THz Bragg waveguide. The gray region and white region represent the high refractive index layer (printing resin) and low refractive index layer (air), respectively. Both the resin and air layer have a thickness of  $512\mu\text{m}$ . The multilayers are kept together with micro-bridge structures distributed uniformly along the waveguide cross section. The number of bilayers is 10. Two mounts at the waveguide periphery are introduced for convenient loading and aligning of the waveguide in the U-shaped holder. The light blue region is a defect layer in the Bragg reflector. (b). Band diagram of the Bragg waveguide with a core diameter of 4.5mm. The yellow solid line illustrates the air light line. Color of each dot indicates the fraction of power guided in the hollow core. The red-colored curve represents the  $\text{HE}_{11}$ -like mode. A typical defect mode due to the presence of the bridges is shown in the insert.

We start by computing the band diagram of the Bragg waveguide with a core diameter much larger than the operation wavelength (1.5mm at 0.2THz), and gradually reduce the core diameter until only the  $\text{HE}_{11}$  mode is guided in the waveguide. In our simulations, the computational cell is terminated by a circular perfect-electric-conducting boundary located at the waveguide periphery. To exclude the modes of a continuum that are concentrated in the vicinity of the numerical boundary, we only present the modes that have more than 30% of the total power confined to an area delimited by a radius equal to the  $2/3$  of that of the waveguide outer boundary. We find that when the waveguide core diameter is reduced to 4.5mm, an effectively single  $\text{HE}_{11}$  mode propagation can be achieved in the fundamental bandgap region (centered at  $\sim 0.18\text{THz}$ ). In Fig. 1(b), we plot the modal effective refractive indices of the guided modes as a function of frequency in the range of 0.1-0.3THz. The color code indicates the fraction of the modal power guided within the hollow core. The blue color defines the modes with power localized mostly outside of the waveguide core, and the red color signals strong presence of the modal fields in the hollow core. The yellow solid line in the diagram is the light line of air with  $n = 1$ . As shown in Fig. 1(b), the bandgap, in fact, features several types of modes that can be identified as core-guided modes and defect modes. The core-guided modes are the two almost degenerate polarizations of the Gaussian-like  $\text{HE}_{11}$  modes [red-colored curves in Fig. 1(b)]. The degeneracy is lifted due to the presence of bridges in the reflector structure. The same bridges lead to appearance of defect modes that are present within the fundamental bandgap. Such modes have less than 20% of their modal power in the core, and they are difficult to excite [see the inset of Fig. 1(b), for example]. Therefore, the Bragg waveguide operates in an effectively single mode regime, when using a linearly polarized Gaussian beam. All the Bragg waveguides used in the following sections have a diameter of 4.5mm, in order to ensure an effectively single- $\text{HE}_{11}$  mode operation.

### 3. Bragg waveguide with a defect layer

It is well known that one can introduce narrow loss peaks into the bandgap region by introducing geometrical defects into the structure of a Bragg reflector [23, 24]. The geometrical defects in the reflector can confine localized states (defect modes) whose frequencies lie within the reflector bandgap. The defect modes can be considered as lossy Fabry-Perot (FP) cavity states localized in the vicinity of the geometrical defects. The optical properties of the FP cavity states are highly sensitive to the thickness of the geometrical defect. Thus, thicker defects (longer FP cavities) result in resonant states at lower frequencies. Similarly, thinner defects result in resonances at higher frequencies. In Bragg waveguides, the geometrical defects can be realized either by thinning a particular reflector layer or by making it thicker. In our experiments, we pursue the latter approach, as thicker layers are easier to realize experimentally due to finite resolution of our 3D printer, as well as mechanical stability considerations when dealing with very thin waveguide layers. As shown in Fig. 1(a), the light blue region represents a defect layer. It is formed by adding material on the inner surface of the waveguide core, which modifies the thickness of the first reflector layer.

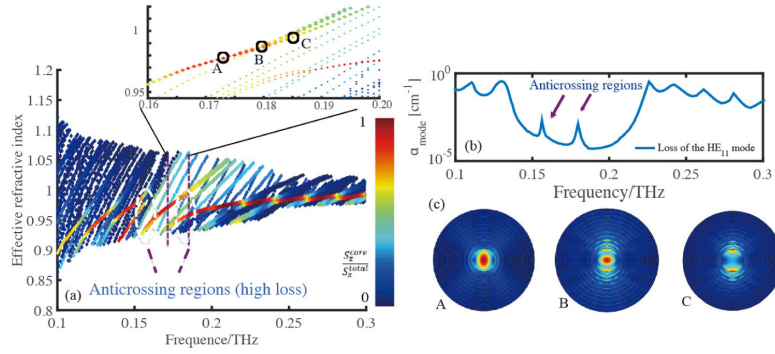


Fig. 2. (a) Band diagram of the Bragg waveguide with a defect layer (thickness: 300 $\mu$ m). The two white dashed ellipses highlight the anticrossing regions between the core-guided mode and the defect modes. Inset: magnified view of the anticrossing region. In order to show the anticrossing phenomenon clearly, we use bigger dots to represent the core-guided HE<sub>11</sub> mode and the defect modes. The black circles refer to the different types of modes guided in the bandgap. (b) Propagation loss of the HE<sub>11</sub> mode. The two sharp loss peaks inside of the bandgap correspond to the two anticrossing regions highlighted as dashed white ellipses in (a). (c) The longitudinal flux distributions for those modes highlighted in the band diagram. A: Core-guided HE<sub>11</sub> mode. B: Hybridized mode. C: Defect modes localized in the immediate vicinity of the defect layer at the waveguide core/reflector interface.

To demonstrate this phenomenon, we compute the band diagram of a Bragg waveguide featuring a defect in the form of a thicker first reflector layer (thickness increase of 300 $\mu$ m). In the simulation, we limit the frequency region to 0.1THz to 0.3THz, where the Bragg waveguide operates in an effectively single HE<sub>11</sub> mode regime. As shown in Fig. 2(a), the introduction of a defect layer into the waveguide core results in anticrossing between the core-guided HE<sub>11</sub> mode and the modes guided predominately in the defect layer. We note that the defect modes are bound to the core/reflector interface, and thus, exhibit significant presence in the lossy cladding material [see mode C in Fig. 2(c)]. Meanwhile, the core-guided mode [see mode A in Fig. 2(c)] has most of the power guided in the low loss air-core region; therefore, its propagation loss is relatively small. Over a certain frequency range, the core-guided mode hybridizes with the defect mode. A hybridized mode is shown as mode B in Fig. 2(c), which is known as the anticrossing phenomenon. Owing to the anticrossing, the dispersion relation of the core-guided mode is significantly altered, as shown in the inset of Fig. 2(a). In the vicinity of the anticrossing frequency, there is a resonant power transfer from the core-guided mode into the defect mode, thus resulting in a significant increase in the

waveguide propagation loss, and thereby resulting in a narrow resonant transmission dip inside the waveguide transmission bandgap. In Fig. 2(b), we present the loss spectrum of the fundamental  $HE_{11}$  mode. As expected, the spectrum features two loss peaks inside of the waveguide bandgap, which correspond to the two anticrossing regions shown in Fig. 2(a).

Thus, by increasing the thickness of the first layer of the reflector, one can introduce guided modes into the defect layer. At the point of anticrossing between the dispersion relations of a lossy defect mode and that of a low-loss core-guided  $HE_{11}$  mode, strong modal hybridization is observed, thereby resulting in strong increase in the propagation loss of the  $HE_{11}$  mode in the vicinity of the anticrossing frequency. The frequency of avoided crossing depends strongly on the defect layer thickness [18]. Therefore, by tracking the shift in the anticrossing frequency (spectral position of the resonant dip), one can build THz waveguide sensors for monitoring changes in the physical/chemical state of the waveguide core surface.

#### 4. THz Bragg waveguides with a perfectly periodic reflector (no defect)

We fabricate the THz Bragg waveguides using a 3D stereolithography system (Pro 2, Asiga), which has a transverse resolution of  $50\mu\text{m}$  and a longitudinal resolution of  $1\mu\text{m}$  (along the waveguide length). We first fabricate five sections of Bragg waveguides with a perfectly periodic reflector (without a defect). Each section has a length of  $2.5\text{cm}$  [see Figs. 3(b)-3(d)].

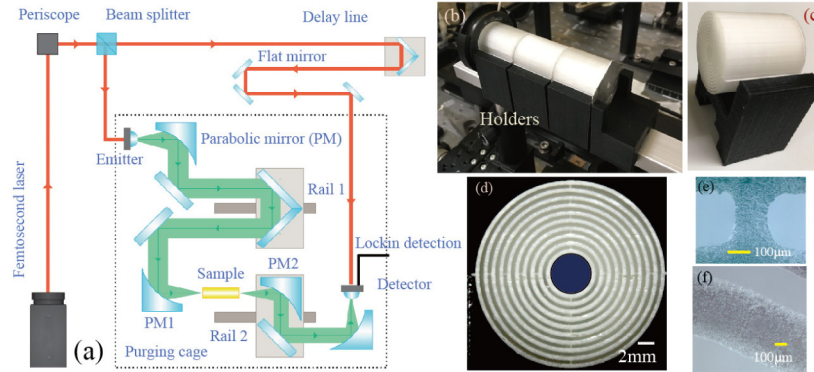


Fig. 3. (a) Schematic of the THz-TDS setup for characterizing the transmission properties of the THz Bragg waveguides. A mirror assembly (rail 2) can translate the output focal plane to accommodate the waveguides of various lengths. The femtosecond laser pulse is shown in red and the THz pulse is shown in green. PM1: fixed parabolic mirror with a focus at the waveguide input facet. PM2: movable parabolic mirror, which is displaced every time when the waveguide section is removed in order to keep the focal point at the waveguide output facet. (b) Three sections of the Bragg waveguides (white) mounted in the U-shaped holders (black). Both the input facet and the output facet of the Bragg waveguides feature an aperture with the size equal to that of the waveguide core. (c) Close-up view of one section of Bragg waveguide mounted in the U-shaped holder. (d) Cross section of the printed Bragg waveguide with a uniformly periodic reflector. (e) Magnified view of the micro-bridge. (f) Magnified view of the high refractive index resin layer.

The transmission spectra are characterized using a terahertz Time Domain Spectroscopy (TDS) setup shown in Fig. 3(a) and detailed in [25]. The setup comprises a frequency doubled femtosecond laser (Ti: Sapphire laser, 90fs, repetition rate of 100MHz, Menlo System) used as a pump source and two identical low-temperature grown GaAs photoconductive antennas used as the THz emitter and detector. A near infrared (NIR) laser pulse is split into two parts by a beam splitter. One part is focused onto a photoconductive emitter for the generation of THz pulse. The THz pulse is then collimated and focused onto the sample by a pair of parabolic mirrors. After passing through the sample, the THz beam is re-collimated and focused onto the detector. The other part of the NIR laser goes through a variable delay line and ultimately terminates on the detector. The delay line allows the THz pulse to be mapped

as a function of time. The photocurrent in the detector is measured with a lock-in amplifier to ensure a good signal-to-noise ratio. The operating frequency range is 0.1-3.0THz. The parabolic mirror that collimates the beam after the sample is mounted on the translation rails. This arrangement allows easy insertion of the THz waveguides and guarantees that both the input facet and the output facet are placed at the focal points of the parabolic mirrors. The Bragg waveguide under test is fixed in a U-shaped holder of equivalent length [see Figs. 3(b) and 3(c)]. The cross section of the fabricated Bragg waveguide with a perfectly periodic reflector is shown in Fig. 3(d). The experimentally measured average thicknesses of the high refractive index resin layer and the micro-bridge are  $512\mu\text{m}$  and  $145\mu\text{m}$  [see Figs. 3(e) and 3(f)], respectively, which are in good agreement with the designed values. The U-shaped holders are mounted on a sliding track, which is placed between the two parabolic mirrors. To prevent excitation of the cladding modes, an iris with a hole-diameter of 4.5mm is fixed at the waveguide input end, and an aluminum foil with a hole-diameter of 4.5mm is glued on the holder at the output facet. The first holder section is fixed in the focal point of the stationary parabolic mirror (PM1), thereby ensuring that the input facet of the Bragg waveguide is also at the focal point of PM1. In the experiment, five holder sections, each hosting a 2.5cm-long waveguide, are removed one by one. During each measurement, the output facet of the holder section (together with the Bragg waveguide) is always fixed in the focal point of the PM2 by adjusting the movable stage. Therefore, waveguides of 12.5cm, 10cm, 7.5cm, 5cm, and 2.5cm are measured. The reference is acquired by removing all the holder sections (together with the waveguide sections), and then moving the PM2 so that the aperture becomes in its focal point.

In Fig. 4, we present the cutback measurements of the transmission spectra through the Bragg waveguides with different lengths. The experimentally measured fundamental bandgap is centered at 0.18THz, which is in good agreement with that of the simulation. Next, the transmission loss of the Bragg waveguide with a uniform reflector is found by comparing the transmission spectra through waveguides of different lengths (cutback method). In Fig. 4(b), we plot the calculated propagation loss of the hollow-core Bragg waveguide in the frequency region between 0.1THz and 0.5THz. We note that, at the fundamental bandgap gap center position (0.18THz), the propagation loss is  $\sim 0.12\text{ cm}^{-1}$ , which is significantly smaller than the corresponding bulk absorption loss of the reflector material at the same frequency ( $\sim 1\text{ cm}^{-1}$ ).

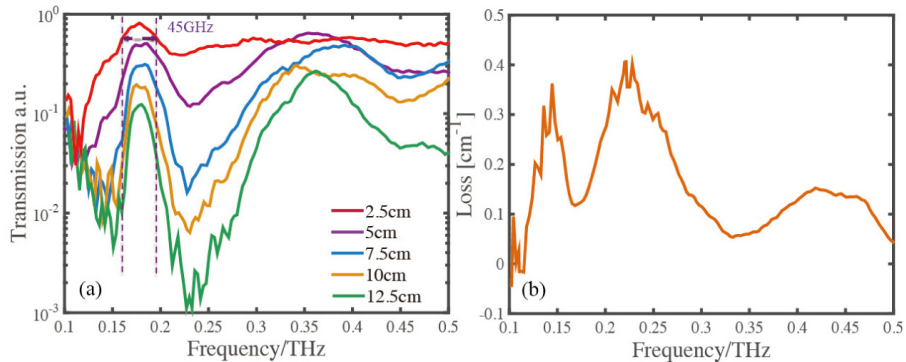


Fig. 4. (a) Measured transmission spectra of the THz Bragg waveguides with uniform periodic reflector for different waveguide lengths (2.5cm, 5cm, 7.5cm, 10cm, and 12.5cm). The bandwidth (FWHM) of the fundamental bandgap of a Bragg waveguide is  $\sim 45\text{GHz}$ . (b) Calculated propagation loss of the hollow-core Bragg waveguide using the cutback method.

## 5. THz Bragg waveguides with a defect layer in the reflector

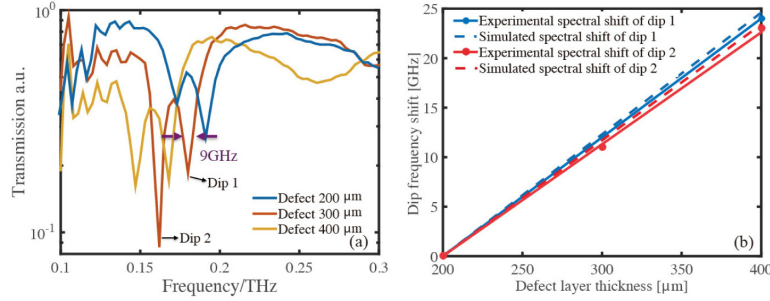


Fig. 5. (a) Measured transmission spectra of the THz Bragg waveguide featuring a defect layer of different thicknesses (200 $\mu\text{m}$ , 300 $\mu\text{m}$ , and 400 $\mu\text{m}$ ). (b) Experimental and theoretical spectral shifts of the two transmission dips as a function of the defect layer thickness.

Next, we introduce narrow resonant loss peaks into the Bragg waveguide transmission spectra by introducing a defect layer with thicknesses of 200 $\mu\text{m}$ , 300 $\mu\text{m}$ , and 400 $\mu\text{m}$ , respectively. Each Bragg waveguide has a length of 2.5cm. Then, we characterize the transmission spectra of the fabricated waveguides with defect layers using the same setup and methodology as presented in Section 4. In Fig. 5(a), we plot the experimentally measured transmission spectra for the Bragg waveguides featuring defect layers of different thicknesses. As predicted, the introduction of a defect layer results in pronounced anticrossings between the core-guided mode and the defect modes localized in the vicinity of the defect layer. The two sharp transmission dips observed in the transmission spectra can be well interpreted by the two anticrossing regions as presented in Fig. 2. When the thickness of the defect layer is increased from 200 $\mu\text{m}$  to 400 $\mu\text{m}$ , the anticrossing frequency shows a blue frequency shift. We note that the two resonant dips in the waveguide transmission spectra correspond to anticrossing of the core-guided mode with the two different defect modes. Generally, due to distinct electric field distributions in these two defect states, we expect that sensitivity of the two resonant peaks to changes in the analyte layer parameters will also be different. In Fig. 5(b), we plot frequency of the two resonant dips found at the right edge (dip 1) and the left edge (dip 2) of the bandgap as a function of the defect layer thickness, and a linear dependency is well observed for both cases. The experimentally obtained surface sensitivity to changes in the thickness of the first reflector layer is found to be 0.12GHz/ $\mu\text{m}$  and 0.115GHz/ $\mu\text{m}$  for the resonant dip 1 and dip2, respectively. The experimental results agree well with the theoretically calculated surface sensitivities of  $\text{HE}_{11}$  mode [see dotted lines in Fig. 5(b)]. In what follows, we use the resonant dip 1 with higher sensitivity in order to perform the sensing of different analytes. Nevertheless, we note that there is alternative sensing modality according to which, one could track changes in the inter-peak spectral separation, rather than the spectral position of one of the two individual peaks. The advantage of the two-peak methodology is that one of the peaks serves as a natural reference for the other one, thus allowing for mitigating various sources of spectral noise. However, in order to make this sensing scheme effective, one has to ensure that the two peaks have significantly different sensitivities to changes of the measurand, thus resulting in appreciable inter-peak spectral changes when analyte optical properties are varied. This implies that the structure of the sensor has to be judiciously designed to realize this condition. Currently, we are investigating the two-peak modality in more details, and we will present our findings in the future works.

The two resonant dips feature narrow linewidths. For example, the linewidth of the transmission dip of the Bragg waveguide with a defect thickness of 300 $\mu\text{m}$  is 9GHz, which is five times smaller than that of the bandgap bandwidth. Additionally, we note that the quoted linewidth of the resonant dip is inferred from the measurements performed using the TDS system, which has a spectral resolution of 3GHz for our system. As we will present later in

Section 9, by using a continuous wave THz spectroscopy setup with sub-1GHz spectral resolution, the actual resonant dip linewidth is much narrower.

## 6. THz Bragg waveguides for monitoring of the optical properties of thin films

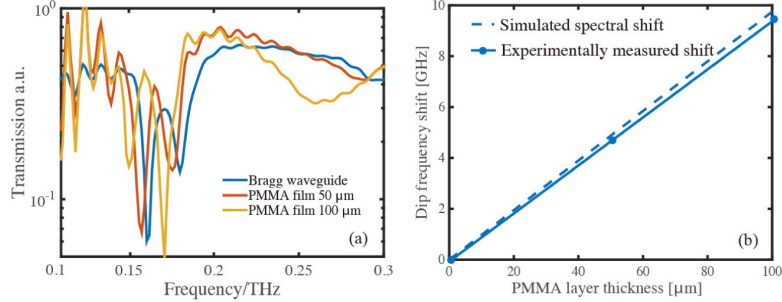


Fig. 6. (a) Measured transmission spectra of the THz Bragg waveguide (with a 300 $\mu$ m defect layer), when PMMA films of different thicknesses (50 $\mu$ m and 100 $\mu$ m) are inserted into the waveguide core. (b) Experimental and theoretical spectral shift of the transmission dip found at the right edge of the bandgap as a function of the PMMA layer thickness.

As a practical demonstration, we apply the proposed THz Bragg waveguide to detect changes in the thickness of a PMMA film attached onto the waveguide inner surface. This is accomplished by tracking the spectral position of the narrow resonance within the Bragg waveguide bandgap. This sensor type can be used, for example, to study degradation of the analyte layer properties due to flow of the reagent vapors or other reactive substances.

We choose the THz Bragg waveguide with a defect layer of 300 $\mu$ m in the Bragg reflector as the sensing platform. In our experiment, PMMA films with two different thicknesses (50 $\mu$ m and 100 $\mu$ m) are manually inserted into the waveguide core. In order to avoid the air gap between the PMMA film and the waveguide core inner surface, we use a rectangular piece of the PMMA film with the length equal to that of the waveguide and the width matched closely to the perimeter of the waveguide core. The PMMA films used in this work are rigid enough to maintain their shapes and adhere tightly to the core inner surface under the stress caused by the round shape of the core. In Fig. 6(a), we plot the experimental transmission spectra of the Bragg waveguides with a PMMA film of different thickness, revealing that, with the increase of the PMMA film thickness, the dip spectral position features a blue frequency shift. In Fig. 6(b), we plot frequency of the resonant dip found at the right edge of the bandgap as a function of the PMMA layer thickness, and a linear dependency is observed. The experimentally achieved surface sensitivity, in this case, is found to be 0.1GHz/ $\mu$ m. We also calculated the surface sensitivity of the HE<sub>11</sub> mode by assuming that the value of the PMMA film refractive index is 1.61 [26]. As shown in Fig. 6(b), the experimental achieved results show a good agreement with our simulation results.

We note that the anticrossing frequency depends on both the thickness and the refractive index of the target analyte. So far, we have investigated the effect of the analyte layer thickness on the sensor response, considering that the analyte refractive index is fixed. An interesting question is whether the current sensor can be modified for the direct measurement of the analyte refractive index. In fact, in order to effectively and reliably extract the refractive index of the target analyte, one would first need to fix the analyte layer thickness and then, calibrate the sensor with various values of analyte refractive indices. However, the major challenge in this approach is how to maintain the same thickness for various analytes during calibration. We note that for liquid and gaseous analytes, their thickness can be fixed via introduction of the well-defined, analyte-filled microfluidic channels into the sensor structure. This is, in fact, a work in progress that we are currently undertaking in our lab, and, we are planning to report on the results in the nearest future.

## 7. THz Bragg waveguides for monitoring of the optical properties of powders

Here, we apply our waveguide sensor to detect thickness changes in the powder analyte, namely,  $\alpha$ -lactose monohydrate (density:  $\sim 1.59\text{g/cm}^3$ , 5989-81-1, Sigma-Aldrich), which is a common excipient in the pharmaceutical and food industry [27]. In the experiment, we choose the THz Bragg waveguide with a defect thickness of  $300\mu\text{m}$  in the first layer of the Bragg reflector as the sensing platform (length:  $2.5\text{cm}$ ). We employ the centrifugal force to disperse the lactose powder analyte onto the waveguide core surface by rotating the waveguide. In particular, as shown in Fig. 7(a), the Bragg waveguide is first clad with a 3D printed tube [black region in Fig. 7(a)] to enhance the mechanical robustness and stability during the fast rotation. The tube is inserted into a bearing (inner diameter: 1 inch; outer diameter: 2 inches), which is fixed into a standard lens mount (inner diameter: 2 inches, LMR2). The rotation of the Bragg waveguide is accomplished by connecting it to a motor via a strap (see Supplementary Visualization 1). During the experiment, in order to prevent the leakage of the lactose powder from the waveguide core during the rotation, an aluminum foil with a hole diameter of  $4.2\text{mm}$  is glued on both the waveguide input and output facets, which is somewhat smaller than the core diameter of the Bragg waveguide ( $4.5\text{mm}$ ).

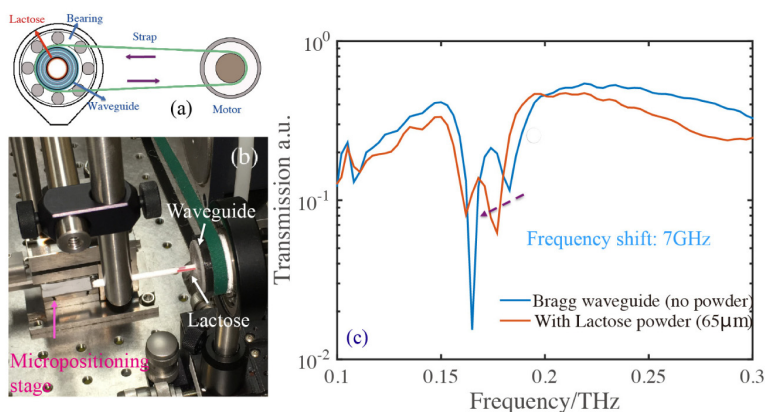


Fig. 7. (a) Schematic of the setup used for monitoring of the thickness of powder analytes deposited on the inner surface of a rotating Bragg waveguide (see Visualization 1). (b) Semi-automatic loader used for feeding lactose powders into the rotating waveguide (see Visualization 2). (c) Measured transmission spectra of the THz Bragg waveguide (with a  $300\mu\text{m}$  defect layer), when  $0.042\text{g}$   $\alpha$ -lactose monohydrate powder analyte (thickness of  $\sim 65\mu\text{m}$ ) is deposited uniformly onto the waveguide inner surface.

In order to ensure formation of uniform lactose films on the waveguide inner surface, we, therefore, pursue several approaches. First, in our setup, we carefully align the waveguide to be as horizontal as possible. Then, during the measurements, we load the lactose powder along the axis of the rotating waveguide using a semi-automatic feeder. During the waveguide rotation, we visually check that the powder has been uniformly dispersed along the waveguide. Beyond the visual inspection we have no means of direct confirmation that the lactose powder is dispersed uniformly. Nevertheless, we are still confident that the resultant film is uniform using an indirect observation method based on the resonant dip width. Particularly, we note that in case of a significant thickness variation of the analyte layer along the waveguide length, the transmission spectrum would feature transmission dips at variable spectral locations related to the local analyte layer thickness. This would result in considerable broadening of the transmission dip. In our experiments both with the low-resolution TDS and the high-resolution CW setups, we do not observe any reliably measurable dip broadening compared to the reference measurement with an empty waveguide. This makes us to conclude that the thus realized power analyte layers are uniform.

In our experiment, we fill the Bragg waveguide core with 0.042g lactose powders, and then, we characterize the transmission spectrum of the waveguide when it is rotated at a speed of 1500RPM (revolutions per minute). As very small amounts of powder are used in the experiment, and the waveguide core size is relatively small, we supplement the basic sensor design with a semi-automatic feeder system [see Fig. 7(b)] that comprises a 3D micro-positioning stage and a straw-like delivery attachment (see Supplementary [Visualization 2](#)). The use of such a feeder is necessary in order to realize a reliable and consistent powder analyte delivery into the sensor. In Fig. 7(c), we present the transmission spectra of the Bragg waveguide sensor before and after dispersing the powder analyte onto the waveguide inner surface. We find that the presence of 0.042g lactose powders causes a frequency shift of 7GHz in the resonant dip position, which reveals a spectral sensitivity of 166GHz/g. In fact, by assuming that the lactose powder is uniformly dispersed onto the waveguide inner surface, the resultant thickness of the lactose film is estimated to be 65 $\mu\text{m}$ , considering that the waveguide has a core diameter of 4.5mm and a length of 2.5cm. In this case, the spectral sensitivity of the Bragg waveguide to changes in the thickness of lactose powders is found to be 0.11GHz/ $\mu\text{m}$ .

In practical industrial applications, in order to capture the target powder analyte onto the waveguide inner surface, one can also pursue the following two approaches: one is to modify the waveguide inner surface with an absorbing layer, which can bind and accumulate specific targets; another alternative is to introduce porous structures into the defect layer. Efficient trapping of micro-particles or powders in the porous structures results in refractive index changes in the defect layer, which can be correlated to the spectral shifts in the resonant dip positions. Furthermore, to enable specific detection of analytes, one can track the specific absorption features that “fingerprint” the analytes. In our case, by designing the operation frequency of the sensor near the absorption peak of  $\alpha$ -lactose monohydrate (at 0.53THz), one could possibly simultaneously monitor the layer thickness and the lactose concentration in the powders using the anticrossing frequency and the absorption peak strength, respectively. This modality, however, has to be further researched.

## 8. Imaging of the modes propagating in the THz Bragg waveguides

To confirm excitation of the defect modes in the vicinity of the anticrossing frequency, we perform the modal imaging at the waveguide output end using a fiber-coupled THz microscopy setup. The schematic of the modal imaging setup is illustrated in Fig. 8(a).

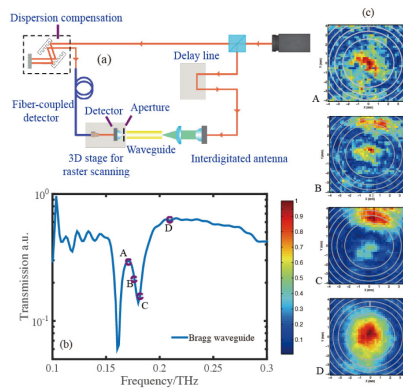


Fig. 8. (a) Schematic of the fiber-coupled THz modal imaging system. (b) Transmission spectrum of the Bragg waveguide (with a 300 $\mu\text{m}$  defect layer). (c) Spatial electric field distribution  $|E_x|$  of the four modes marked in (b) acquired at the output of the waveguide.

A photoconductive antenna is used as the detector, and a free space coupled high power interdigitated antenna is used as the emitter. The photoconductive antenna has a silicon lens

and an aperture of 1mm mounted in front of the lens. In order to compensate the pump pulse broadening due to the dispersion in the fiber, a grating-based, dispersion-compensation system is used before coupling the near-infrared pulse into the polarization-maintaining fiber [28]. The output end of the fiber is placed on a 3D stage, and a fiber collimator is used to couple the output of the fiber into free space to excite the detection antenna. The detection antenna is raster scanned with a step resolution of 250 $\mu\text{m}$  across the output end of a waveguide to perform the modal imaging. Because the photoconductive antenna is only sensitive to the polarization parallel to the dipole electrode, we only measure the spatial electric field distributions ( $|E_x|$ ) in this experiment.

A Bragg waveguide (with a defect thickness of 300 $\mu\text{m}$ ) is used in this experiment. In Fig. 8(b), we plot the transmission spectrum of the waveguide measured using the TDS system. In Fig. 8(c), we plot the spatial electric field distributions of the four modes marked in Fig. 8(b). As expected from the simulation results, in the vicinity of the anticrossing frequency, the core-guided mode (mode A) hybridizes with the defect mode (mode C). Mode B is a hybridized mode. We note that the asymmetric profile of the defect mode is probably due to a misalignment and off-center coupling of the THz beam to the Bragg waveguide in the experiment. As the frequency moves far from the anticrossing region, the modal profile becomes a Gaussian shape in the electric field distribution, which agrees well with the HE<sub>11</sub> mode structure. This confirms an effectively single-HE<sub>11</sub>-mode propagation in the fundamental bandgap region of the Bragg waveguide.

## 9. Resolution enhancement using continuous wave THz spectroscopy

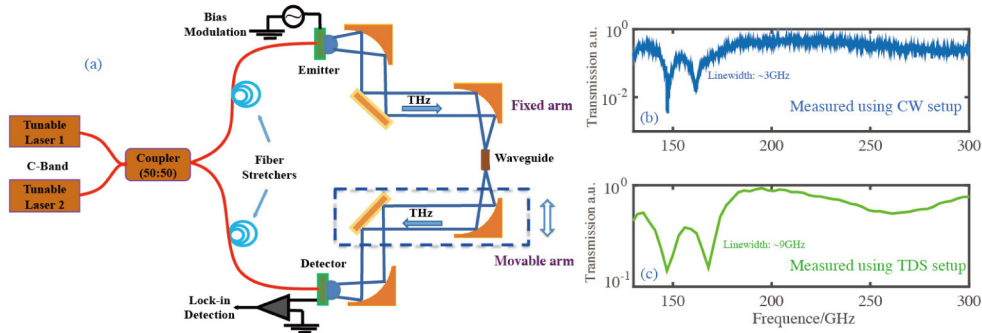


Fig. 9. (a) Schematic of the THz-CW spectroscopy setup for characterizing the transmission spectra of the THz Bragg waveguides. Comparison of the transmission spectra of the Bragg waveguide (with a 400 $\mu\text{m}$  defect layer) measured using (b) THz-TDS and (c) THz-CW setups.

In a THz-TDS setup, the frequency resolution of the Fourier transform of a THz waveform is fundamentally limited by the span of the time delay sweep, which, in turn, is typically limited to 200-300ps due to appearance of echoes in the THz time trace. These are caused by the multiple reflections in the silicon lens and antenna substrates. In a typical THz-TDS setup, the resolution is, therefore, limited to  $\sim 1$ -3GHz [29], thus setting the sensor detection limit.

Continuous wave terahertz spectroscopy systems based on the photo-mixing effect constitute a viable alternative to the TDS systems for high-resolution spectral characterizations. The CW-terahertz generation is based on heterodyne difference frequency generation in the high-bandwidth photoconductors: The beat signal of the two lasers is converted into a CW-terahertz wave exactly at the difference frequency of the lasers. In comparison to time-domain terahertz systems, a CW-terahertz setup enables spectrally selective measurements and, at the same time, offers a significantly improved frequency resolution and signal power. The frequency resolution of CW systems is determined by the linewidth of the laser sources, which is typically in the 10MHz range [30]. Finally, the cost of such systems is comparable to the cost of the TDS systems.

For comparison, in this section we characterize the transmission spectra of the hollow-core Bragg waveguide sensor using a continuous wave terahertz spectroscopy system from Toptica Photonics. The schematic illustration of this setup is shown in Fig. 9(a). The setup has two distributed feedback (DFB) lasers with slightly different center wavelengths and balanced power ( $\sim 30\text{mW}$  for each laser) operating in the telecommunication range. A 50:50 coupler combines and splits the two wavelengths equally into the emitter and detector arms. In order to measure the phase information, each arm features a fiber stretcher. The two stretchers operate with opposite signs, thus enhancing the optical path difference. Each fiber stretcher consists of a polarization-maintaining single-mode fiber wound around a piezo actuator. The generated THz waves are modulated with a bias voltage for lock-in detection.

In Fig. 9(b), we plot the transmission spectrum of a Bragg waveguide (with defect thickness of  $400\mu\text{m}$ ) measured using the CW system with a reliable resolution of  $40\text{MHz}$ . For comparison, we also plot the spectrum of the same waveguide characterized using the TDS setup in Fig. 9(c) with time traces of  $300\text{ps}$ . Overall, the spectrum of the Bragg waveguide sensor measured using the CW setup shows good agreement with that measured using the TDS setup. More importantly, we note that the linewidth of the resonant dip characterized by the CW setup is only  $3\text{GHz}$ , which is much narrower than that measured using the TDS setup ( $9\text{GHz}$ ). The corresponding Q factor of the sensor is therefore 55. Although the quality factor of the resonant dip is not the highest for a sensor operating in the THz range [31], the  $3\text{GHz}$  linewidth, to the best of our knowledge, is among the narrowest measured for any resonator in the THz range [32–34]. With the experimentally demonstrated sensitivity of  $0.1\text{GHz}/\mu\text{m}$  and narrow linewidth of the spectral features, our Bragg waveguide sensor can be used for the detection of targets with size ranging from  $\sim 100\text{nm}$  to hundreds of microns by considering that the practical frequency resolution of a continuous wave THz setup is in the  $10\text{MHz}$  range. This is of great significance for biosensing applications, when precision detection of targets, such as bacteria, cell, and other macro-molecular layers, is needed.

## 10. Sensor detection limit for powder analytes using the THz-CW setup

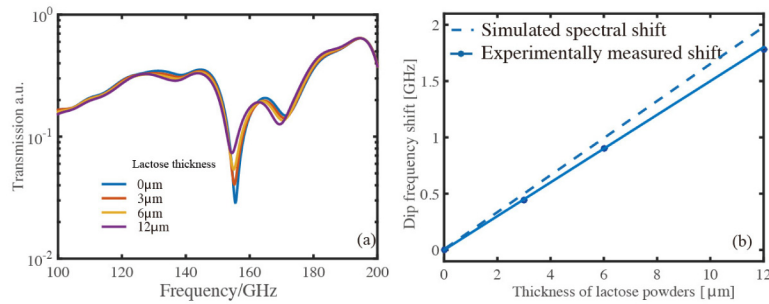


Fig. 10. (a) Measured transmission spectra of the THz Bragg waveguide (with a  $300\mu\text{m}$  defect), when different amounts of lactose powders are loaded into the core (corresponding analyte layer thicknesses are  $0\mu\text{m}$ ,  $3\mu\text{m}$ ,  $6\mu\text{m}$ ,  $12\mu\text{m}$ ). (b) Experimental and theoretical spectral shift of the transmission dip found at the right edge of the bandgap as a function of the layer thickness.

We now evaluate the detection limit of the resonant Bragg waveguide sensors when used for monitoring thickness of the powder analytes. In this study, we employ the continuous wave THz setup that offers high spectral resolution in order to resolve minute changes in the sensor spectral response when loading small amounts of lactose powders. Particularly, the powder is introduced in small amounts with mass increments of  $0.002\text{g}$  (corresponding thickness increase is  $3\mu\text{m}$ ) into the rotating Bragg waveguide using a semi-automatic feeder described earlier. Totally, three measurements are performed for the net masses of the lactose powder equal to  $0.002\text{g}$ ,  $0.004\text{g}$ , and  $0.008\text{g}$  that correspond to the analyte layer thicknesses of the  $3\mu\text{m}$ ,  $6\mu\text{m}$ , and  $12\mu\text{m}$  on the inner core surface.

In Fig. 10(a), we present the transmission spectra of the Bragg waveguide sensor before and after dispersing the powders onto the waveguide inner surface. We note that in order to resolve the minute spectral shifts caused by the small amounts of lactose powders, we perform the Fourier transform of the transmission spectra of the waveguide sensor and remove the high frequency fluctuations in the signal that arises due to the standing waves between the waveguide facet and the detector. We find that the increase of lactose powder mass causes a continuous frequency shift in the resonant dip positions. In Fig. 10(b), we plot frequency of the resonant dip found at the right edge of the bandgap as a function of the lactose layer thickness, and a linear dependency is observed. The experimentally achieved surface sensitivity is found to be  $0.14\text{GHz}/\mu\text{m}$ , which is somewhat higher than that we have achieved using the TDS setup. This is probably due to the enhanced spectral resolution of the CW setup. Moreover, in order to theoretically validate the experimental results, we also calculate the surface sensitivity of the  $\text{HE}_{11}$  mode. The refractive index of the  $\alpha$ -lactose monohydrate is found in [35] as is taken to be 1.78 in our simulations. The theoretical surface sensitivity of the Bragg waveguide sensor is shown in Fig. 10(b) and we observe a good agreement between the theoretical and experimental results.

## 11. Discussions

### 11.1. Comparison of the waveguide sensor to free space transmission mode THz spectroscopy for thin film sensing

Thin film characterization using THz waves is recognized as an important technique, which has many practical applications. Thin films that are particularly relevant in the development of high-speed electronics [36] include epitaxial semiconductors, dielectric insulators, and graphene, among others. Biosensing is another field where thin film detection is of great significance. Target substances such as bacteria, cells, monolayers, or ligands, are typically studied in the form of thin films on top of functionalized substrates [37].

One of the simplest configurations used for THz thin film sensing is based on a free space transmission mode spectroscopy [38]. Changes in a thin dielectric film can be detected by observing the phase variations in the transmission spectrum. However, this technique has many fundamental and practical challenges. Since thin samples offer a very short interaction length in such configurations, they only impart little modifications to the waves passing through it. The measurement accuracy is significantly reduced, when the measurement uncertainties become relatively strong compared to the phase changes induced by the samples. Only if the confidence intervals of the sample and reference measurement are well separated, can it then be inferred that a sample is reliably detected [38]. It is reported that a THz transmission mode spectroscopy system can be used to detect thin polymer films with thickness down to  $\sim 2\mu\text{m}$  by observing the phase change between the averaged reference and sample measurements. However, in practice, for reasonable accurate characterization, it is recommended that the thin film thickness be at least ten times above this limit.

The lack of resonant interaction between the THz waves and the samples is the principal factor that limits the resolution of conventional transmission mode spectroscopy. In our THz waveguide sensor, the modal field in the core is resonantly coupled to the field in the defect mode in the anticrossing spectral region. The resonant dip with narrow linewidth in the waveguide transmission spectrum can be used to resolve minute spectral shifts in the resonant dip positions caused by small changes in the defect layer thickness or refractive index, which allows an improved detection limit, compared to that of the conventional transmission mode spectroscopy setups. With the experimental demonstrated sensitivity of  $0.1\text{GHz}/\mu\text{m}$  and a reliable spectral resolution of  $40\text{MHz}$  in our CW setup, the THz Bragg waveguide sensor can be used for the sensing of thin films with sub-micron thicknesses ( $400\text{nm}$ ).

### 11.2. Practical applications of the THz waveguide sensors

Currently, THz sensing of powder analytes has been extensively applied for the discovery of illicit drugs [39], and explosive or hazardous powders [40] via their fingerprint THz spectra. The presented THz Bragg waveguide sensor could potentially distinguish various powders if a selective binding of specific powders to the waveguide inner surface could be realized, or, when the sensor is operated in the vicinity of the spectral “fingerprint” absorption lines. Other potential applications of the waveguide sensors include industrial or environmental pollution detection, as well as monitoring of dynamical generation of solid or liquid compounds in chemical reactions. For example, ammonia gas interacts with hydrochloric acid, producing particles of chloride ammonium. Moreover, such waveguide sensors can be used for monitoring the precipitation of objects on the core surface, thickness variations due to flow of reagent vapors, and changes in the layer refractive index caused by chemical process. Finally, the proposed THz Bragg waveguide sensor could also be used as a viable platform for efficient and label-free detection of bacteria pathogens. By functionalizing the surface of the waveguide core with specific phages, selective detection of pathogenic bacteria could be realized with the proposed THz Bragg waveguide sensor. Changes in the resonant dip positions could be directly correlated with the concentration of bacteria samples. These are all the new exciting directions that we are currently exploring in our laboratories.

## 12. Conclusions

In this paper, we propose using 3D printed hollow-core THz Bragg waveguides with defect layers for resonant surface sensing applications. It is demonstrated that by introducing a defect into the first layer of the Bragg reflector, a strong and spectrally narrow dip appears in the waveguide transmission spectrum. The dip is due to the anticrossing phenomenon between the core-guided mode and a mode localized in the defect of the Bragg reflector. By tracking the anticrossing frequency, which manifests itself as a transmission dip with narrow linewidth in the waveguide transmission spectrum, one can detect changes in the geometrical or optical properties of the defect layer. Both the THz-TDS and THz-CW setups are used in our work, and we conclude that CW setup with higher frequency resolution is more suitable for applications that require high sensitivities. The experimentally achieved linewidth of the resonant dip (with a THz CW setup) is only 3GHz, which is among the narrowest measured for any resonator in the THz range. As a practical demonstration, we apply this sensor for detecting PMMA films with different thicknesses loaded on the inner surface of the waveguide core. Target film thickness can be directly correlated to the position of the anticrossing frequency. A surface sensitivity of 0.1GHz/ $\mu\text{m}$  is achieved experimentally. Moreover, an example of THz resonant surface sensing using  $\alpha$ -lactose monohydrate powder as the analyte is demonstrated experimentally using a setup with rotating waveguide, where the powders are spread uniformly on the waveguide core surface via the action of centrifugal force. We demonstrate that our sensor is capable of reliable detection of 3 $\mu\text{m}$  change in the analyte layer thickness, which is among the lowest ever reported for THz sensing. Finally, the anticrossing phenomenon between the core-guided mode and the defect mode is directly confirmed by imaging the modes propagated in the waveguide using a THz microscopy setup.

### Appendix: THz optical properties of the resin used in 3D stereolithography

The refractive index and absorption losses of the reflector material used in the Bragg waveguide fabrication are characterized using a THz-TDS setup. Cutback measurements are performed using three printed resin slices of 6mm thickness. In the experiment, the printed resin slices are fixed on a holder [see Fig. 11(a)], which is placed between the two parabolic mirrors. The resin slices have the same thickness with flatness on the sub-50 $\mu\text{m}$  scale. During the cutback measurements, the slices are placed tightly close to each other so as to minimize the air gap between them (due to surface roughness), which in any case remains

deeply sub-wavelength. Also, we note that on the top of each slice a small notch is present in order to simplify the removal of the slides during measurements. The outmost left resin slice is fixed in the focal point of the parabolic mirror (PM1), while the outmost right resin slice is fixed at the focal point of the parabolic mirror (PM2). To ensure constant coupling conditions during measurements, resin slices are removed one by one from the right. Thus, transmission spectra through resin samples with different thicknesses (18mm, 12mm, 6mm) are measured.

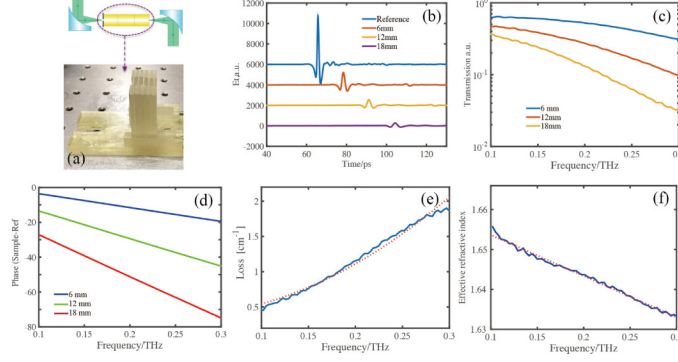


Fig. 11. Optical characterizations of the photosensitive resin using cutback method. (a) 3D printed resin samples of various lengths mounted in the holder. (b) Temporal traces of the THz pulses at the output of the resin slices (plotted with a vertical offset for clarity), (c) transmission spectra, (d) unwrapped phases (relative to the reference), (e) resin absorption loss and the polynomial fit ( $p = 2$ ), (f) resin refractive index and the polynomial fit ( $p = 1$ ).

We note that PM2 is fixed in this measurement. In each measurement, 20 traces are recorded and averaged in order to enhance the signal-to-noise ratio. The real part of the resin refractive index and the absorption coefficient are extracted from the measured complex transmission data. Following [41–44], the measured complex transmission is given by:

$$T(\omega, L) = \frac{E_t}{E_r} = |T(\omega, L)| \cdot \exp[i\varphi(\omega, L)]$$

$$|T(\omega, L)| = C_{in} \cdot C_{out} \cdot \exp\left[-\frac{\alpha(\omega) \cdot L}{2}\right]$$

$$\varphi(\omega, L) = -\frac{\omega}{c}(n_r(\omega) - 1) \cdot L$$
(1)

where  $E_t$  and  $E_r$  are the complex transmission spectra measured with a sample of length  $L$  and a reference (all samples removed).  $C_{in}$  and  $C_{out}$  represent the input and output coupling coefficients of the THz light, which are assumed to be same during all the measurements.  $n(\omega)$ , and  $\alpha(\omega)$  are the real part of the refractive index, and the absorption coefficient of the samples. We note that, the THz spectroscopic measurements are performed in focused beam geometry, while the standard routine for the retrieval of the sample refractive index assumes plane-wave approximation, we therefore, use the model proposed in [44], in order to correct the Gouy shift for a more accurate determination of the refractive index of the resin. In Fig. 11(b), we show the temporal traces of the THz pulses guided through the resin slices with different thicknesses (traces are plot with a vertical offset for clarity). For each slice with a different length, the temporal delay compared to the reference pulse is proportional to the slice thickness. In Figs. 11(c) and 11(d), we plot the transmission spectra and the unwrapped phases relative to the reference of the tested samples of different thicknesses. Our analysis is limited to the frequency range of 0.1-0.3THz, where all the spectra are well above the noise

level. In this frequency range, the absorption coefficient and the refractive index can then be fitted using second order and first order polynomials as:

$$\alpha(\omega)[\text{cm}^{-1}] = 0.64 + 13.44 \cdot (\omega[\text{THz}])^2, \quad (2)$$

$$n(\omega) = 1.654 - 0.07\omega[\text{THz}]. \quad (3)$$